Journal of Materials Chemistry A

RSC Publishing

PAPER

View Article Online
View Journal



# Zinc alloyed iron pyrite ternary nanocrystals for band gap broadening†

Cite this: DOI: 10.1039/c3ta11039g

Baodong Mao,[a] Qingfeng Dong,[a] Zhengguo Xiao,[a] Christopher L. Exstrom,[b] Scott A. Darveau,[b] Thomas E. Webber,[b] Bjorn D. Lund,[b] Hui Huang,[c] Zhenhui Kang[c] and Jinsong Huang*[a]

Received 12th March 2013
Accepted 16th July 2013

DOI: 10.1039/c3ta11039g

www.rsc.org/MaterialsA

Iron pyrite ($FeS_2$) is one of the most promising photovoltaic materials with high natural abundance and low cost but with a lower-than-optimum band gap of 0.95 eV. Here the feasibility of band gap broadening was explored by zinc alloying of $FeS_2$ nanocrystals (NCs). A significant amount of zinc up to 6 at%, 30 times higher than previously reported, was incorporated into the $FeS_2$ NCs. In contrast to band gap bowing predicted by first-principles calculations, a band gap enlargement of ~0.1 eV was observed by zinc alloying. A more than five-times reduction of dark current in the zinc alloyed $FeS_2$ photoconductor was observed and should ascribe to the increased band gap.

## Introduction

One attractive strategy to dramatically lower the cost of photovoltaic (PV) energy conversion is to develop highly efficient PV cells using naturally abundant materials and low-cost solution fabrication methods. Iron pyrite ($FeS_2$) is one of the most promising next-generation PV materials due to its high abundance and nontoxicity.[1] Its high absorption coefficient (~$5 \times 10^5$ $cm^{-1}$) enables sufficient light absorption by ultrathin films (<200 nm).[1,2] These characteristics rank $FeS_2$ as the top candidate in terms of extraction costs and supply constraints in a series of unconventional semiconductor material systems that potentially lead to low cost and sustainable PV materials.[2] With the fast development of nanocrystal (NC)-based inks for printable solar cells in the last decade,[3,4] pyrite NCs with better crystallinity and well controlled size and shape have attracted much research interest[5–14] due to the ease of operation and low cost by dip-, spin- and spray-coating.[15–17]

The iron pyrite band gap of 0.95 eV is small enough to absorb a broad solar spectrum, but is far below the theoretical optimum band gap (1.34 eV) to produce a single junction PV device with highest efficiency.[18] Enlarging the band gap of iron pyrite by alloying with either suitable anions ($FeA_xS_{2-x}$, where A is an anion element such as O, As, *etc.*) or cations ($M_xFe_{1-x}S_2$, where M is a cation element such as Zn, Ru, *etc.*) has been theoretically evaluated widely.[19,20] Although anion alloying with oxygen has been proposed to increase the band-gap of $FeS_2$,[19,21] cation alloying is more controllable experimentally. To identify a suitable cation element for alloying, factors including material abundance, environment impact and cost need to be considered so the advantages of using pyrite as the PV material will not be negated. Although iron pyrite alloys with Ru and Os are predicted to have a larger band gap by Sun's recent first principles calculations,[20] these elements are not naturally abundant. In contrast to the profound theoretical study on alloying of iron pyrite, only a few experimental studies have been reported including Co-,[22] $Sn^{4+}$-,[23] Ni-, Co-, As-,[24] and Zn-alloyed $FeS_2$.[25] Among all the elements that can alloy with iron pyrite to increase the band gap, Zn holds the highest promise because of its earth abundance and low cost. Furthermore, zinc is an element widely used for doping and surface coating of semiconductor NCs due to the stability and unique electronic properties of zinc chalcogenides.[26,27] $ZnS_2$ has a band-gap of 2.0–2.5 eV,[20,28] and thus the band gap of zinc alloyed iron pyrite ($Zn_xFe_{1-x}S_2$) can be continuously tuned from 0.95 to 2.5 eV if the whole alloying composition range can be achieved. However there are two challenges associated with Zn alloyed iron pyrite for band gap broadening: (1) $Zn_xFe_{1-x}S_2$ alloy system is predicted to have large band-gap bowing effects by Sun's recent first principles calculations,[20] *e.g.* the band gap is even lower than that of $FeS_2$ with a small percentage of incorporated Zn; (2) although $ZnS_2$ and pyrite $FeS_2$ have the same unit cell structure, there is a challenge to incorporate relatively high percentages of zinc into iron pyrite due to the size difference of $Zn^{2+}$ (0.74 Å) and $Fe^{2+}$ (0.61 Å), which might impose an energy barrier for the

[a]Department of Mechanical and Materials Engineering, University of Nebraska-Lincoln, Lincoln, Nebraska 68588, USA. E-mail: jhuang2@unl.edu; Fax: +1-4024721465; Tel: +1-4024722640

[b]Department of Chemistry, University of Nebraska at Kearney, Kearney, Nebraska 68849, USA

[c]Institute of Functional Nano and Soft Materials (FUNSOM), Jiangsu Key Laboratory for Carbon-Based Functional Materials and Devices, Soochow University, Suzhou, China

† Electronic supplementary information (ESI) available: Complete XRD patterns, summary of lattice parameters, elemental mapping and TEM images of $Zn_xFe_{1-x}S_2$ NCs synthesized with other parameters. See DOI: 10.1039/c3ta11039g

dynamics process. Previous attempts to alloy Zn with bulk $FeS_2$ by a chemical vapor transport method have not shown successful incorporation of Zn yielding a very low doping concentration (200 ppm), which eventually did not cause noticeable band gap variation.[25]

It is possible to incorporate higher levels of dopants into NCs by releasing the lattice strain to the surface if the NCs are within the critical size of strain release.[29,30] In the present work, the feasibility of Zn alloyed $FeS_2$ ternary NCs was explored experimentally in an effort to increase the band gap towards the optimal for an improved PV performance. The formation of $Zn_xFe_{1-x}S_2$ NCs was investigated using XRD, Raman spectroscopy and elemental analysis. Zn incorporation percentages up to 6 at% were achieved and resulted in an increased band gap to 1.32 eV. The effect of zinc alloying was also evaluated for construction of photodetector devices using the $Zn_xFe_{1-x}S_2$ NCs.

## Experimental

### Materials

Anhydrous iron(II) chloride ($FeCl_2$, 99.9%), zinc stearate ($Zn(C_{18}H_{37}COO)_2$,·98%), zinc acetate ($Zn(CH_3COO)_2 \cdot 2H_2O$, >97%), sulfur (98%), trioctylphosphine oxide (TOPO, 90%), oleylamine (OLA, 70%), chloroform (99.8%), anhydrous methanol, ethanedithiol (EDT), and acetonitrile (99.8%) were purchased from Sigma-Aldrich. Isopropanol (IPA) and ethanol were acquired from VWR. All chemicals were used without further purification.

### Synthesis of $Zn_xFe_{1-x}S_2$ alloyed NCs

The synthetic procedure is a modified hot-injection method based on our previously reported $FeS_2$ NC synthesis.[6] The starting Zn/(Fe + Zn) precursor ratio ($Zn_s$) was tuned from 0 to 50% in order to tune the composition of $Zn_xFe_{1-x}S_2$. For $Zn_s$ = 10%, 0.45 mmol $FeCl_2$, 0.05 mmol zinc stearate, 0.3 mmol TOPO, and 10 mL OLA were degassed at 120 °C under vacuum for 1 h to remove oxygen and water. The mixture solution was further refluxed at 170 °C for 2 h under nitrogen protection to form the Fe–OLA complex. After that, the solution temperature was increased to 220 °C and 5 mL of 0.6 M S/OLA solution was injected. A higher injection temperature compared to previous methods was chosen to ensure the simultaneous sulfurization of Fe and Zn precursors because of the lower formation temperature of iron sulfides than zinc sulfides.[5,6] Finally, the reaction system was kept at this temperature for another 2 h to ensure the growth of $Zn_xFe_{1-x}S_2$ NCs. Other $Zn_xFe_{1-x}S_2$ NCs were also synthesized with increasing zinc alloying level ($x$ value) under the same synthetic conditions but with varying $Zn_s$ in the precursor. Zinc acetate was also used in the synthesis instead of zinc stearate, in which the amount of all chemicals was doubled, *e.g.* 1 mmol of (Fe + Zn), 20 mL OLA, 0.6 mmol TOPO and 10 mL of 0.6 M S/OLA solution were used.

After cooling down to room temperature, the $Zn_xFe_{1-x}S_2$ NCs were precipitated out by adding IPA and centrifugation. The $Zn_xFe_{1-x}S_2$ NCs were washed with toluene/IPA, toluene/IPA, and chloroform/methanol and redispersed in chloroform. The NCs/chloroform dispersions were stored in a $N_2$ filled glove box for further characterization and device fabrication.

### Characterizations

The phase of the $Zn_xFe_{1-x}S_2$ NCs was determined by powder X-ray diffraction (XRD) using a Rigaku D/Max-B diffractometer (Co K$\alpha$, $\lambda$ = 1.79026 Å). Raman spectra were recorded using a Renishaw Confocal Raman Microscope with a 514 nm laser to further investigate the phase evolution with increasing zinc. The size and morphology of the NCs were studied using transmission electron microscopy (TEM, Hitachi H7500) with an accelerating voltage of 100 kV. Energy-dispersive X-ray spectroscopy (EDX) and elemental mapping were conducted using an FEI/Philips Tecnai 12 BioTWIN TEM operated at 200 kV with EDX analyses. Absorption spectra of the $Zn_xFe_{1-x}S_2$ NCs were recorded using a PerkinElmer Lambda 900 UV/VIS/NIR spectrometer. The composition of the NCs, *e.g.* Zn/Fe ratio, was measured by inductively coupled plasma atomic emission spectroscopy (ICP-AES). The film thickness was measured using an Ambios technology XP stylus profiler.

### Device fabrication and measurements

The $Zn_xFe_{1-x}S_2$ photovoltaic devices have the structure of ITO/ZnO/$Zn_xFe_{1-x}S_2$/$MoO_3$/Au/Ag.[15] A cleaned indium tin oxide (ITO) glass substrate was treated by ultraviolet–ozone for 10 min. The ZnO NCs were synthesized by a hydrolysis method using zinc acetate and KOH in methanol described elsewhere.[31–33] The ZnO NC layer was spin coated with 50 mg $mL^{-1}$ ZnO NCs/$CHCl_3$ solution at 3000 rpm for 50 s and then annealed at 200 °C for 10 min in air to form a high quality ZnO film with a thickness of 90 nm. The active layer of $Zn_xFe_{1-x}S_2$ NCs was formed by spin-coating with 10 mg $mL^{-1}$ NCs/$CHCl_3$ solution at 2500 rpm for 30 s. After spin-coating, the thin films were treated with 1% ethanedithiol (EDT)/acetonitrile solution for 15 s, spin dried at 2500 rpm, and washed with acetonitrile, allowing ligand exchange by the short chain EDT molecules and formation of high quality thin film devices. After that, the $MoO_3$(10 nm)/Au(20 nm)/Ag(80 nm) layers were deposited sequentially by thermal evaporation under vacuum. A thin gold layer was used to avoid the reaction of $Zn_xFe_{1-x}S_2$ with the silver electrode and to improve the stability of the devices. The final active device area was approximately 0.075 $cm^2$. The photocurrent was measured using a Keithley 2400 source meter under simulated sunlight of air mass 1.5 (100 mW $cm^{-2}$).

## Results and discussion

XRD was used first to verify the incorporation of zinc into the $FeS_2$ lattice after the reaction, and then to determine whether any byproducts such as ZnS formed in the reaction. Fig. 1a shows the XRD patterns of the $Zn_xFe_{1-x}S_2$ NCs formed with different $Zn_s$. Only three strongest peaks are shown here to demonstrate the peak shift with zinc incorporation and complete XRD patterns are given in Fig. S1 in the ESI.† The XRD patterns basically follow that pyrite structure (JCPDS no. 42-1340), and no noticeable impurity peak was observed. The shift

 

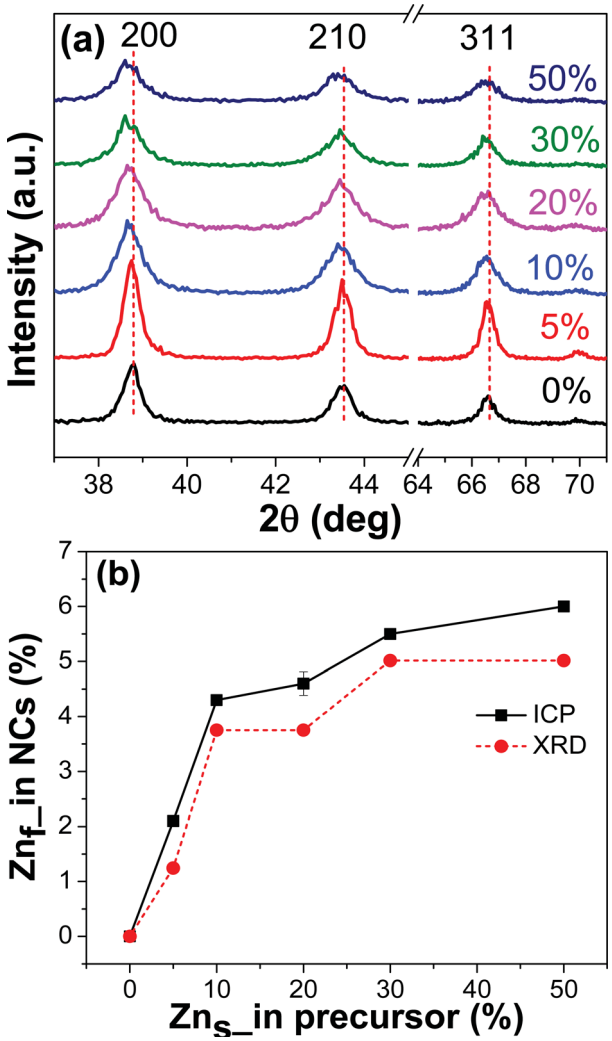


**Fig. 1** (a) XRD pattern of the $Zn_xFe_{1-x}S_2$ NCs synthesized with different starting ratios of zinc in the precursors; (b) atomic ratio of zinc in the NCs estimated from XRD peak shifts (red) and measured by ICP-AES (black).

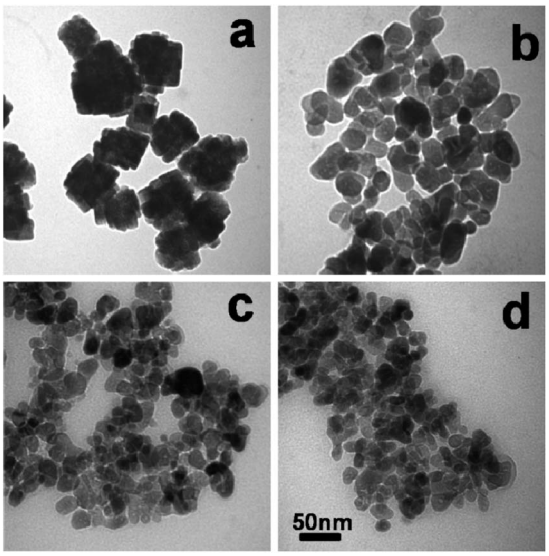


**Fig. 2** TEM images of the $Zn_xFe_{1-x}S_2$ NCs synthesized with different starting zinc ratios in the precursor: (a) $Zn_s = 0\%$, $60 \pm 14.1$ nm; (b) $Zn_s = 5\%$, $30 \pm 5.5$ nm; (c) $Zn_s = 20\%$, $24 \pm 5.9$ nm; and (d) $Zn_s = 50\%$, $19 \pm 6.5$ nm.

of all the XRD peaks to smaller diffraction angles also excludes the formation of ZnS, because all main diffraction peaks of ZnS locate close to but at the larger diffraction angles than those peaks of iron pyrite. The main diffraction peaks show a slight broadening and shift to the smaller diffraction angles with an increasing amount of Zn in the precursor. The peak broadening may be mainly ascribed to the size decrease of the NCs with an increasing zinc amount (Fig. 2, as discussed below). The (200) peak shifts from 38.80 to 38.60°, the (210) peak shifts from 43.55 to 43.40° and the (311) peak shifts from 66.60 to 66.35°. This agrees with our expectation that the incorporation of zinc into pyrite would result in the increase of the lattice constants, because $ZnS_2$ has a larger lattice constant. The crystal lattice constants ($a_0$) are 5.416 Å for $FeS_2$ and 5.954 Å for $ZnS_2$.[20]

The lattice parameters ($a_0$) of the $Zn_xFe_{1-x}S_2$ NCs were calculated using the (200), (210), and (311) diffraction peaks and are summarized in Table S1.† The lattice parameter ($a_0$) of 5.416 Å is frequently ascribed to $FeS_2$ in recent studies.[20] The lattice parameters of our doped NCs with $Zn_s < 20\%$, 5.399 to 5.409 Å, are all smaller than the standard (5.416 Å), and the other two samples with $Zn_s = 30\%$ and 50% are slightly larger than the standard. One reason might be the relatively small size (20–60 nm) resulting from the structural disorder on the NC surface. It was also reported that the reduced S deficiency from 13% to 0% can also result in the increase of lattice parameter from 5.416 to 5.428 Å.[34] However, even for the undoped $FeS_2$ NCs in our work, the S : Fe ratio is as high as 6 : 1, similar to most of the solution synthesis routes to ensure the formation of iron pyrite. EDX measurements indicated that with $Zn_s = 0\%$, 5%, 20% to 50%, the S : (Fe + Zn) ratio changes from 2.15, 2.07, 2.17 to 2.06, suggesting that there is no obvious sulfur deficiency or nonstoichiometry in the $Zn_xFe_{1-x}S_2$ NCs considering an accuracy of 5% in the EDX measurement. Also the S : metal ratio does not show any noticeable trend of increase with increasing zinc and decreasing iron amounts. Another important reason is that such S-deficient structures generally have much higher conductivity, while ours show lower dark current.

The final percentage of zinc incorporation ($Zn_f$) can be estimated from the changed crystal plane space, which can be derived from the changed diffraction angle using the Bragg's law as follows:

$$\frac{\Delta d}{d} = \frac{1}{\tan(\theta)}\Delta\theta \quad (1)$$

where $d$ is the crystal plane spacing and $\theta$ is the diffraction angle. By assuming a linear relationship between the lattice constant change and the incorporated Zn percentage, the final zinc ratios ($Zn_f$) estimated from the (200) peak shifts are 1.25 at%, 3.75 at%, 3.75 at%, 5.02 at% and 5.02 at% with $Zn_s$ increase from 5% to 50% as summarized in Fig. 1b (red circle curve). This is roughly consistent with the composition measurement by inductively coupled plasma atomic emission spectroscopy (ICP-AES) that is described below.

The accurate element composition of the $Zn_xFe_{1-x}S_2$ NCs measured using ICP-AES is summarized in Fig. 1b (black square curve). With a low zinc ratio ($Zn_s$ < 10%) in the precursor, the final ratio of zinc in the NCs increased quickly from 2.1% ($Zn_s$ = 5%) to 4.3% ($Zn_s$ = 10%) with a roughly linear relationship between $Zn_s$ and $Zn_f$. The linearity was lost with the further increased $Zn_s$. The zinc alloying level was increased to 6.0% in the $Fe_xZn_{1-x}S_2$ NCs with the starting zinc concentration of 50%. Replacing zinc stearate with zinc acetate with a $Zn_s$ of 50% gives a $Zn_f$ of 6.2 at%, which did not show any dramatic improvement of the alloying level and indicated that the stearate ligand is not the limiting factor of the alloying level. The restricted alloying level may be due to the miscibility problem of $FeS_2$ and $ZnS_2$ caused by the differences in the electronegativity (1.65 of Zn *vs.* 1.83 of Fe) and the ionic radius (0.74 Å *vs.* 0.61 Å of $Fe^{2+}$) between zinc and iron.[20] It is not rare that the dopants' concentration in the NCs is an order of magnitude less than that in the precursor solutions.[29,35,36] It should be noted that this is the first time that Zn is successfully alloyed with iron pyrite at a considerable concentration, and 6 at% is the highest reported Zn incorporation percentage reported to date.[25] It is expected that the strain brought about by the incorporated large Zn ion[37] is easier to be released to the surface in small size and large surface area NCs than in bulk materials or two dimensional thin films, which allows high level alloying. Furthermore, elemental mapping of the $Zn_xFe_{1-x}S_2$ NCs was carried out and is shown in Fig. S2.† The distribution of zinc atoms is basically the same as that of S and Fe. The zinc signal shows a lower signal/noise ratio due to the ~5% zinc alloying level.

There are two possible paths for the remaining zinc precursors: staying in solution as a molecular complex or forming small sized ZnS NCs that were not precipitated out together with larger $Zn_xFe_{1-x}S_2$ NCs. Firstly, it is possible that not the entire zinc precursor reacted because the temperature employed here (220 °C) is not likely to be high enough for complete precipitation of zinc to ZnS in an oleylamine/trioctylphosphine oxide solvent system. While 4 nm ZnS nanoparticles have been prepared by the reaction of $ZnCl_2$ and sulfur in oleylamine at 210 °C,[38] in reported syntheses of ZnS in oleylamine with either trioctylphosphine oxide (TOPO) or trioctylphosphine (TOP) as a co-surfactant, high temperatures of 280–320 °C (ref. 39 and 40) were employed in order to overcome the nanoparticle nucleation activation energy brought about by the formation of fairly stable Zn–TOPO and Zn–TOP solution complexes. Secondly, if the small sized ZnS NCs formed, they might be discarded during washing with chloroform/methanol. To precipitate the $Zn_xFe_{1-x}S_2$ NCs out with the good solvent (chloroform here) during washing, the poor solvent (methanol here) was used as little as possible to avoid aggregation of the $FeS_2$ NCs.[13,41] The ratio of methanol : chloroform employed in our work is 1 : 1. It is possible that the small sized ZnS NCs, if formed, were still left in the solution and were decanted later, while the larger $Zn_xFe_{1-x}S_2$ NCs were precipitated out with methanol.

TEM was used to characterize the size and morphology of the $Zn_xFe_{1-x}S_2$ NCs as shown in Fig. 2. The increase of the zinc ratio resulted in a smoother surface of the NCs and also in a smaller particle size, which decreased from 60 nm ($Zn_s$ = 0%), 30 nm ($Zn_s$ = 5%), 24 nm ($Zn_s$ = 20%) to 19 nm ($Zn_s$ = = 50%). This is consistent with the observed XRD peak broadening shown in Fig. 1. The NCs also changed from quasi-cubic to quasi-spherical with zinc alloying. The decreasing NC size and change of the NC shape can be explained by the fact that the increased Zn content in the ternary alloy induces more lattice distortion and strain to be released to the NC surface, which restricts the NC size increase and prevents the cubic facet formation. It is difficult to grow large sized NCs with more Zn because the critical NC size for strain release decreases with more strain introduced. When zinc stearate was replaced with zinc acetate, even smaller sized $Zn_xFe_{1-x}S_2$ NCs (<10 nm, Fig. S3†) formed but are easy to aggregate to larger particles, which further indicated the important role of the stearate ligand that provided stronger protection for the growing NCs. On the other hand, in an attempt to obtain sharp edge nanocubes with higher crystallinity,[6] reducing the injection temperature to 170 °C yielded the co-existed big (>100 nm) nanocubes and small (~10 nm) spherical NCs (Fig. S4†), so it was not adopted in further experiments. The high injection temperature (220 °C) is required to match the reactivity of Zn and Fe so that Zn can be

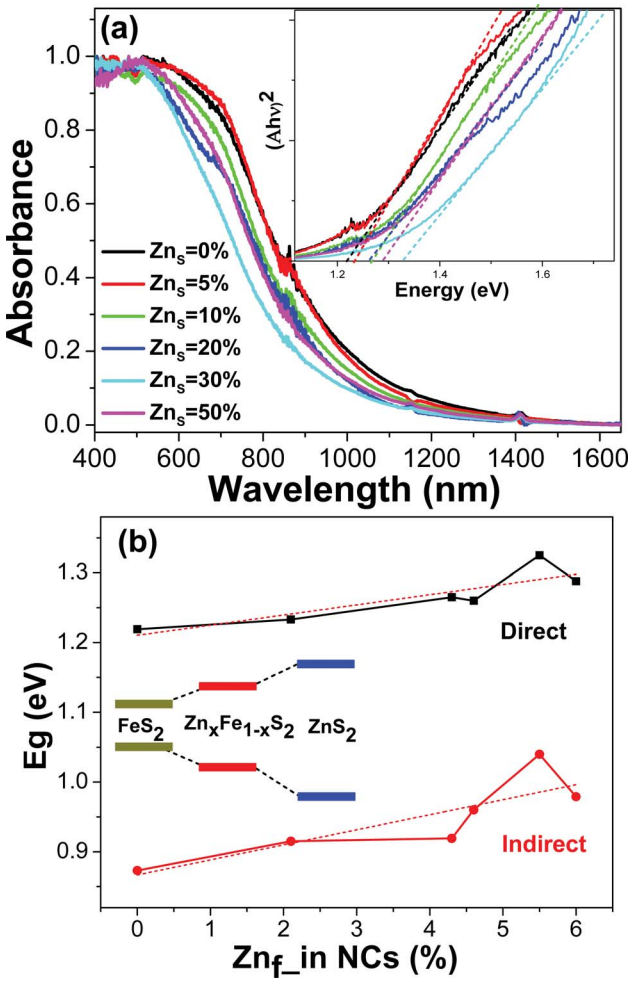


**Fig. 3** (a) UV-vis-NIR absorption spectra of the $Zn_xFe_{1-x}S_2$ NCs. The inset shows the estimation of direct optical band gaps. (b) The direct and indirect band gaps changing with the actual zinc atomic ratio measured from ICP.

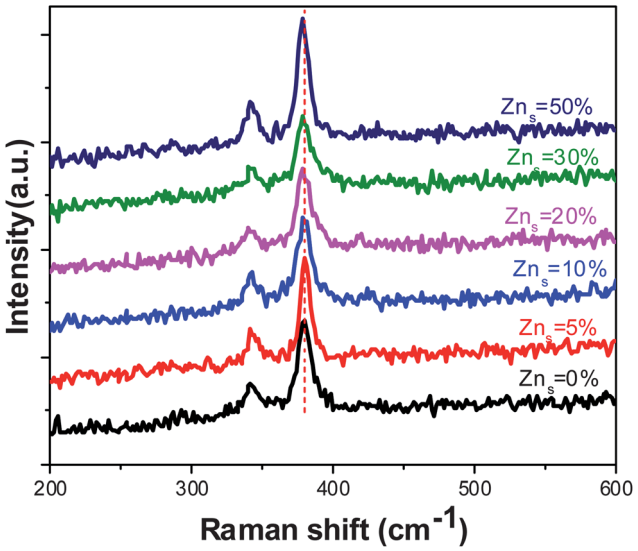


**Fig. 4** Raman spectra of the $Zn_xFe_{1-x}S_2$ NCs synthesized with different starting ratios of zinc in the precursors.

incorporated into $FeS_2$ simultaneously with NC growth. Comprehensive consideration of the above aspects including precursor ratio, capping ligands, and temperature is required to obtain high quality alloyed $Zn_xFe_{1-x}S_2$ NCs.

The optical absorption spectra of the synthesized $Zn_xFe_{1-x}S_2$ NCs were measured and are shown in Fig. 3a. The absorption spectra showed continuous blue shifts with increasing incorporated Zn percentage. This result clearly demonstrates the feasibility of band gap broadening of iron pyrite through zinc alloying. The small peaks or valleys around 1150 and 1410 nm are due to the background absorption of chloroform. The direct optical band gaps were calculated from the absorption curve of $(\alpha h\nu)^2$ *vs.* $h\nu$ (inset of Fig. 3a), which increased from 1.219 eV to 1.325 eV with $Zn_f$ = 5.5 at%, close to the ideal band gap of 1.34 eV for single-junction PV cells.[18] The band gap of the $Zn_xFe_{1-x}S_2$ NCs increases with increasing incorporated zinc in a roughly linear manner as shown in Fig. 3b, which can be simply described by Vegard's law.[42] The indirect band gap of the $Zn_xFe_{1-x}S_2$ NCs increases similarly from 0.873 to 1.04 eV (Fig. 3b, red curve). Although band gap calculation using absorption spectra suffers from the problems of scattering and particle aggregation,[9,13] it was also reported that the band gap of $FeS_2$ NCs from absorption spectra is consistent with the direct methods of X-ray absorption and emission.[13] Our band gap results are in direct contrast to the band gap bowing effect of Zn doped iron pyrite predicted by first-principles calculations.[20]

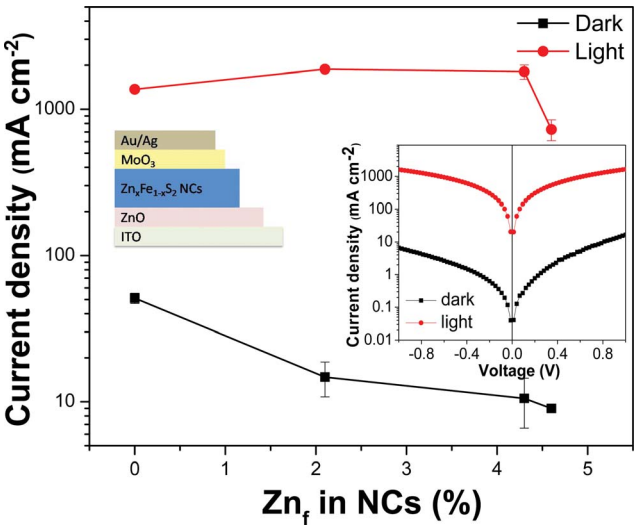


**Fig. 5** Photocurrent and dark current changes of the $Zn_xFe_{1-x}S_2$ NC photodetector devices with different zinc alloying levels with the structure of ITO/ZnO/$Zn_xFe_{1-x}S_2$/$MoO_3$/Au/Ag with a bias of −1 V. The insets show a schematic structure of the $Zn_xFe_{1-x}S_2$ photodetector devices (left) and typical dark current and photocurrent curves of a $Zn_{0.043}Fe_{0.957}S_2$ NC device (right).

The structure evolution of the $Zn_xFe_{1-x}S_2$ NCs with increasing Zn incorporation ratio was further investigated using Raman spectroscopy. As shown in Fig. 4, the pure pyrite NCs show two Raman peaks around 340 and 380 $cm^{-1}$, which can be labeled as the well-defined $E_g$ and $A_g$ modes of pyrite, respectively.[43–45] The $A_g$ mode Raman peak corresponds to in-phase stretching vibrations of the S–S dimeric units,[43,44] and the vibrational mode $E_g$ is mainly governed by the Fe–S force constant.[45] No noticeable Raman peak was observed for ZnS in the range of 200–600 $cm^{-1}$, again verifying the absence of ZnS or marcasite in the final reaction product. With increasing Zn incorporation ratio, the $A_g$ mode peak showed a red shift of about 2.4 $cm^{-1}$ from 380.1 to 378.7 $cm^{-1}$, while no clear shift trend of the $E_g$ mode peak at 340 $cm^{-1}$ was observed. The decrease of the frequency of $A_g$ mode indicates the increase of the S–S bond length with Zn incorporation,[14,34] which is consistent with the increase of the lattice parameter observed in XRD after alloying.

Finally, the synthesized $Zn_xFe_{1-x}S_2$ NCs were evaluated for the application of photodetector devices with a device structure of ITO/ZnO/$Zn_xFe_{1-x}S_2$/$MoO_3$/Au/Ag.[15] As shown in the right inset of Fig. 5, the devices showed a good photoconductive response but no photovoltage was similar to recently reported iron pyrite devices.[15,17] An important observation in our devices is that the dark current decreases with increasing zinc incorporation percentage. For a quick comparison, with a bias of −1 V, the dark current decreases from 51.1 to 9.0 mA $cm^{-2}$, with increasing zinc percentage from 0% to 4.6% as shown in Fig. 5. This result agrees with the expectation that an increased band gap of the semiconductor gives a lower density of thermally activated free charges and thus lower dark current. With the slightly increased photocurrent and dramatically reduced dark current, the incorporation of the Zn into iron pyrite resulted in a large increase of on/off ratio, which is important for photodetector application.[15] PV devices with improved efficiency may be expected with further optimization of device design and fabrication using high quality $Zn_xFe_{1-x}S_2$ NCs with reduced density of defects.

## Conclusions

In summary, zinc alloying of iron pyrite NCs was investigated for band gap broadening. An improved alloying level up to 6 at% was achieved with comprehensive consideration of precursor

ratio, capping ligands, and temperature. Crystal lattice enlargement was observed and correlated well with the Zn incorporation ratio. The band gap of the $Zn_xFe_{1-x}S_2$ NCs increases with increasing zinc alloying level in a roughly linear manner and no band gap bowing was observed. An increased photoresponse with zinc alloying was observed in the $Zn_xFe_{1-x}S_2$ NC devices resulting from the reduced dark current that was related to defect states.

## Acknowledgements

J. H. acknowledges the financial support from Nebraska Public Power District through the Nebraska Center for Energy Sciences Research and Nebraska Research Initiative.

## Notes and references

1 A. Ennaoui, S. Fiechter, C. Pettenkofer, N. Alonsovante, K. Buker, M. Bronold, C. Hopfner and H. Tributsch, *Sol. Energy Mater. Sol. Cells*, 1993, **29**, 289–370.
2 C. Wadia, A. P. Alivisatos and D. M. Kammen, *Environ. Sci. Technol.*, 2009, **43**, 2072–2077.
3 P. V. Kamat, *J. Phys. Chem. C*, 2008, **112**, 18737–18753.
4 I. J. Kramer and E. H. Sargent, *ACS Nano*, 2011, **5**, 8506–8514.
5 J. Puthussery, S. Seefeld, N. Berry, M. Gibbs and M. Law, *J. Am. Chem. Soc.*, 2011, **133**, 716–719.
6 Y. Bi, Y. B. Yuan, C. L. Exstrom, S. A. Darveau and J. S. Huang, *Nano Lett.*, 2011, **11**, 4953–4957.
7 C. Wadia, Y. Wu, S. Gul, S. K. Volkman, J. H. Guo and A. P. Alivisatos, *Chem. Mater.*, 2009, **21**, 2568–2570.
8 L. Zhu, B. Richardson, J. Tanumihardja and Q. M. Yu, *CrystEngComm*, 2012, **14**, 4188–4195.
9 B. X. Yuan, W. L. Luan and S. T. Tu, *Dalton Trans.*, 2012, **41**, 772–776.
10 H. A. Macpherson and C. R. Stoldt, *ACS Nano*, 2012, **6**, 8940–8949.
11 M. Akhtar, J. Akhter, M. A. Malik, P. O'Brien, F. Tuna, J. Raftery and M. Helliwell, *J. Mater. Chem.*, 2011, **21**, 9737–9745.
12 Y. J. Zhang, Y. P. Du, H. R. Xu and Q. B. Wang, *CrystEngComm*, 2010, **12**, 3658–3663.
13 J. M. Lucas, C.-C. Tuan, S. D. Lounis, D. K. Britt, R. Qiao, W. Yang, A. Lanzara and A. P. Alivisatos, *Chem. Mater.*, 2013, **25**, 1615–1620.
14 M. Caban-Acevedo, D. Liang, K. S. Chew, J. P. DeGrave, N. S. Kaiser and S. Jin, *ACS Nano*, 2013, **7**, 1731–1739.
15 D. Y. Wang, Y. T. Jiang, C. C. Lin, S. S. Li, Y. T. Wang, C. C. Chen and C. W. Chen, *Adv. Mater.*, 2012, **24**, 3415–3420.
16 Y. Y. Lin, D. Y. Wang, H. C. Yen, H. L. Chen, C. C. Chen, C. M. Chen, C. Y. Tang and C. W. Chen, *Nanotechnology*, 2009, **20**, 405207.
17 C. Steinhagen, T. B. Harvey, C. J. Stolle, J. Harris and B. A. Korgel, *J. Phys. Chem. Lett.*, 2012, **3**, 2352–2356.
18 W. Shockley and H. J. Queisser, *J. Appl. Phys.*, 1961, **32**, 510–519.
19 J. Hu, Y. N. Zhang, M. Law and R. Q. Wu, *J. Am. Chem. Soc.*, 2012, **134**, 13216–13219.
20 R. S. Sun and G. Ceder, *Phys. Rev. B: Condens. Matter Mater. Phys.*, 2011, **84**, 245211.
21 R. S. Sun, M. K. Y. Chan, S. Y. Kang and G. Ceder, *Phys. Rev. B: Condens. Matter Mater. Phys.*, 2011, **84**, 035212.
22 B. Thomas, K. Ellmer, W. Bohne, J. Rohrich, M. Kunst and H. Tributsch, *Solid State Commun.*, 1999, **111**, 235–240.
23 J. Xia, X. H. Lu, W. Gao, J. Q. Jiao, H. J. Feng and L. P. Chen, *Electrochim. Acta*, 2011, **56**, 6932–6939.
24 S. W. Lehner, N. Newman, M. van Schilfgaarde, S. Bandyopadhyay, K. Savage and P. R. Buseck, *J. Appl. Phys.*, 2012, **111**, 083717.
25 K. Buker, S. Fiechter, V. Eyert and H. Tributsch, *J. Electrochem. Soc.*, 1999, **146**, 261–265.
26 S. S. Lo, T. Mirkovic, C. H. Chuang, C. Burda and G. D. Scholes, *Adv. Mater.*, 2011, **23**, 180–197.
27 X. S. Fang, T. Y. Zhai, U. K. Gautam, L. Li, L. M. Wu, B. Yoshio and D. Golberg, *Prog. Mater. Sci.*, 2011, **56**, 175–287.
28 D. W. Bullett, *J. Phys. C: Solid State Phys.*, 1982, **15**, 6163–6174.
29 D. J. Norris, A. L. Efros and S. C. Erwin, *Science*, 2008, **319**, 1776–1779.
30 R. Beaulac, S. Ochsenbein and D. Gamelin, in *Nanocrystal Quantum Dots*, ed. V. I. Klimov, CRC Press, 2010, pp. 397–453.
31 F. W. Guo, B. Yang, Y. B. Yuan, Z. G. Xiao, Q. F. Dong, Y. Bi and J. S. Huang, *Nat. Nanotechnol.*, 2012, **7**, 798–802.
32 J. P. Liu, S. C. Qu, X. B. Zeng, Y. Xu, X. F. Gou, Z. J. Wang, H. Y. Zhou and Z. G. Wang, *Appl. Surf. Sci.*, 2007, **253**, 7506–7509.
33 C. Pacholski, A. Kornowski and H. Weller, *Angew. Chem., Int. Ed.*, 2002, **41**, 1188–1191.
34 C. delasHeras, J. L. M. deVidales, I. J. Ferrer and C. Sanchez, *J. Mater. Res.*, 1996, **11**, 211–220.
35 R. S. Selinsky, J. H. Han, E. A. Morales Perez, I. A. Guzei and S. Jin, *J. Am. Chem. Soc.*, 2010, **132**, 15997–16005.
36 B. D. Mao, C. H. Chuang, F. Lu, L. X. Sang, J. J. Zhu and C. Burda, *J. Phys. Chem. C*, 2013, **117**, 648–656.
37 R. D. Shannon, *Acta Crystallogr., Sect. A: Cryst. Phys., Diffr., Theor. Gen. Crystallogr.*, 1976, **32**, 751–767.
38 G. Kremser, T. Rath, B. Kunert, M. Edler, G. Fritz-Popovski, R. Resel, I. Letofsky-Papst, W. Grogger and G. Trimmel, *J. Colloid Interface Sci.*, 2012, **369**, 154–159.
39 H. T. Zhang, B. R. Hyun, F. W. Wise and R. D. Robinson, *Nano Lett.*, 2012, **12**, 5856–5860.
40 J. Joo, H. B. Na, T. Yu, J. H. Yu, Y. W. Kim, F. X. Wu, J. Z. Zhang and T. Hyeon, *J. Am. Chem. Soc.*, 2003, **125**, 11100–11105.
41 W. Li, M. Doblinger, A. Vaneski, A. L. Rogach, F. Jackel and J. Feldmann, *J. Mater. Chem.*, 2011, **21**, 17946–17952.
42 L. Vegard, *Z. Physik*, 1921, **5**, 17–26.
43 A. K. Kleppe and A. P. Jephcoat, *Mineral. Mag.*, 2004, **68**, 433–441.
44 H. Vogt, T. Chattopadhyay and H. J. Stolz, *J. Phys. Chem. Solids*, 1983, **44**, 869–873.
45 M. Blanchard, M. Alfredsson, J. Brodholt, G. D. Price, K. Wright and C. R. A. Catlow, *J. Phys. Chem. B*, 2005, **109**, 22067–22073.

 